Drug Design, Development and Therapy

Dovepress
Taylor & Francis Group

Open Access Full Text Article

ORIGINAL RESEARCH

# Uncovering Thyroid Vulnerability to Doxorubicin: Integrative Cellular and in vivo Evidence of Mitochondrial Dysfunction

Weiqiang Huang[1,*], Yongpan Wang[1,*], Hanbing Wang[2], Rongbing Chen[3], Haiqing Gu[1], Shunyan Yu[1], Ziwei Bao[4], Li Luo[5], Da Sun[6], Binjiao Zheng[7]

[1]Thyroid and Breast Surgery, The First People`s Hospital of Jiashan, Jiashan Hospital Affiliated to Jiaxing University, Jiaxing, 314100, People's Republic of China; [2]Department of Biotechnology, The University of Hong Kong, Hong Kong SAR, 999077, People's Republic of China; [3]Department of Biomedical Engineering, City University of Hong Kong, Hong Kong SAR, 999077, People's Republic of China; [4]Internal Medicine Residency Training Base, The Affiliated Guangdong Second Provincial General Hospital of Jinan University, Guangzhou, Guangdong, 510310, People's Republic of China; [5]National Engineering Research Center of Cell Growth Factor Drugs and Protein Biologics, Wenzhou Medical University, Wenzhou, 325000, People's Republic of China; [6]Institute of Life Sciences & Biomedical Collaborative Innovation Center of Zhejiang Province, Wenzhou University, Wenzhou, 325035, People's Republic of China; [7]Key Laboratory of Laboratory Medicine, Ministry of Education, Zhejiang Provincial Key Laboratory of Medical Genetics, School of Laboratory Medicine and Life Sciences, Wenzhou Medical University, Wenzhou, Zhejiang, 325035, People's Republic of China

*These authors contributed equally to this work

Correspondence: Da Sun; Binjiao Zheng, Email sunday@wzu.edu.cn; gusdy13x@wmu.edu.cn



**Objective:** Doxorubicin (DOX), a first-line anthracycline chemotherapeutic for triple-negative breast cancer (TNBC), is known to cause severe off-target toxicities including cardiotoxicity. However, its effects on the thyroid, a key regulator of systemic metabolism and long-term health, have been largely overlooked. Our study addresses this gap by investigating whether DOX directly impairs thyroid integrity and elucidating the underlying mechanisms.

**Materials and Methods:** An integrated experimental strategy was employed, combining primary mouse thyroid follicular epithelial (MTFE) cells, zebrafish (AB strain) larvae, and multidisciplinary molecular and histopathological approaches. To better simulate the physiological context of chemotherapy, MTFE cells were exposed to DOX that had been effluxed from TNBC cells. Oxidative stress, mitochondrial function, and apoptotic activity were assessed in MTFE cells, while zebrafish larvae were treated with DOX to evaluate thyroid hormone secretion, inflammatory cytokine levels, and fibrotic changes. Key biomarkers were analyzed via immunofluorescence and histological staining.

**Results:** In MTFE cells, DOX triggered significant oxidative stress, reflected by elevated malondialdehyde (MDA) levels, and led to mitochondrial dysfunction, evidenced by ultrastructural abnormalities and loss of JC-1 membrane potential. In zebrafish, DOX exposure resulted in an approximately 20% reduction in T3/T4 levels, accompanied by a 1.4-fold increase in TNF-α, indicating that the hormone shift serves as a marker of inflammatory thyroid injury. These findings establish a direct link between DOX-induced oxidative and mitochondrial damage and the structural and functional deterioration of thyroid tissue.

**Conclusion:** Our findings reveal a previously underappreciated thyrotoxic effect of DOX, primarily mediated via oxidative stress-driven mitochondrial dysfunction and apoptotic signaling. These insights underscore the novelty of the thyroid as a vulnerable target during DOX-based chemotherapy and emphasize the need for routine thyroid monitoring in clinical practice. This work further supports developing adjunct interventions to mitigate thyroid damage and improve long-term safety in cancer survivors.

**Keywords:** DOX-induced toxicity, injury of thyroid, follicular thyroid, oxidative stress, mitochondrial damage

## Introduction

Doxorubicin (DOX) is a potent chemotherapeutic agent and exhibits significant efficacy in the management of diverse malignancies, including triple-negative breast cancer (TNBC).[1] Its anti-tumor activity is mediated by multiple biological

https://doi.org/10.2147/DDDT.S576622
Received: 24 October 2025
Accepted: 12 February 2026
Published: 25 February 2026

**Graphical Abstract**

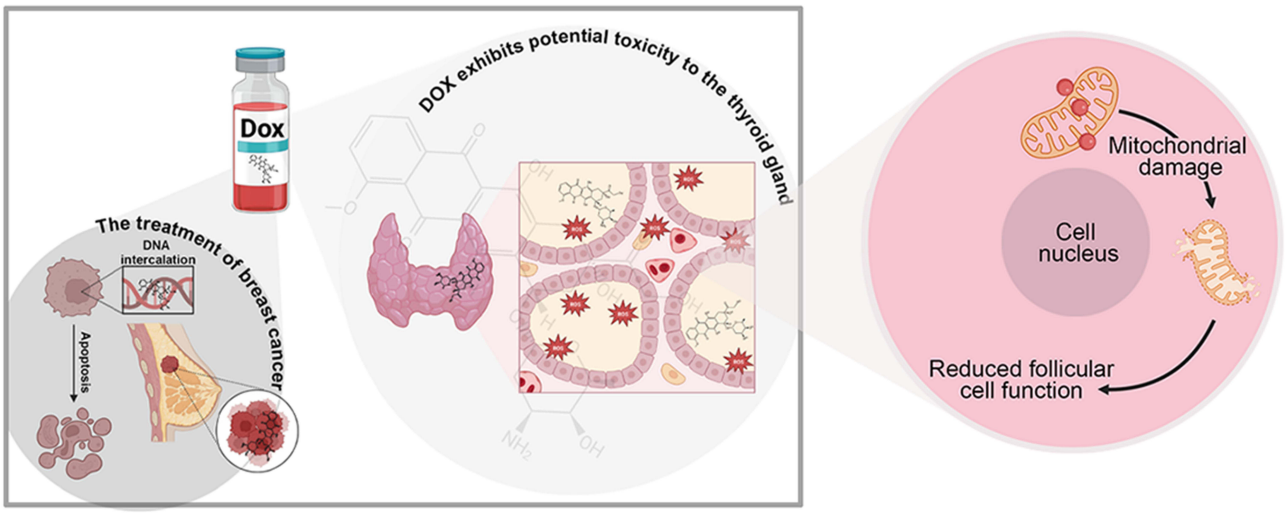


pathways, including its intercalation into DNA strands, suppression of transcriptional processes via topoisomerase II inhibition, and induction of cell death through reactive oxygen species (ROS) generation.[2,3]

Nevertheless, the clinical utility of DOX is limited by its well-documented off-target toxicities, particularly when administered at high cumulative doses.[4] Although DOX is rapidly cleared from plasma following intravenous administration (with a half-life of approximately 5~10 minutes), it extensively accumulates in metabolically active organs such as the liver, spleen, kidneys, lungs, and heart.[5,6] This unique pharmacokinetic property of DOX enables it to induce toxic damage to normal tissues even as it exerts its anti-tumor effects.[7] Specifically, the toxic side effects of DOX primarily manifest as: (1) myelosuppression, the most common dose-limiting toxicity, which presents as significant reductions in peripheral blood platelet and white blood cell counts, with severe cases carrying an increased risk of infection or bleeding; (2) cardiotoxicity, notable for its delayed onset (typically emerging weeks to months after treatment initiation), leading to mitochondrial dysfunction in cardiomyocytes, exacerbated oxidative stress, and in severe instances, progression to heart failure (occurring in approximately 5~10% of patients); (3) gastrointestinal toxicity, including nausea, vomiting, abdominal pain, and oral mucosal ulcers (affecting 30~50% of patients), which are mostly transient but significantly impair quality of life; and (4) other toxicities such as alopecia (reversible upon discontinuation), fever, hemorrhagic erythema, and hepatic dysfunction (eg, elevated transaminases).[8–10]

The thyroid gland, as a central endocrine organ, synthesizes and secretes thyroid hormones (THs) essential for systemic metabolism, growth, and development.[11,12] Drug-induced thyroid dysfunction (DITD) occurs when medications interfere with thyroid hormone synthesis, secretion, or regulation by thyrotropin (TSH), leading to hypo- or hyperthyroidism, thyroiditis, or other abnormalities.[13–15] This includes conditions such as hypothyroidism, hyperthyroidism, autoimmune thyroiditis, and destructive thyroiditis. Commonly implicated drugs in DITD are categorized into six major classes: (1) antineoplastic agents; (2) iodine-containing medications (eg, amiodarone); (3) lithium salts; (4) glucocorticoids; (5) non-steroidal anti-inflammatory drugs (NSAIDs); and (6) certain central nervous system agents. Cancer patients represent a particularly vulnerable population for thyroid dysfunction.[16–18] Given this high prevalence, a comprehensive understanding of the impact of antineoplastic drugs on thyroid function during cancer treatment is of critical clinical importance.

No previous studies have systematically examined the thyroid as a potential target organ of DOX toxicity. Considering the thyroid's pivotal role in systemic metabolism and the frequent occurrence of thyroid dysfunction in cancer patients, addressing this gap is essential to improve therapeutic safety and patient quality of life.[19,20] Several

clinical and biological factors complicate the attribution of thyroid dysfunction solely to DOX.[21] First, concomitant administration of other medications (eg, amiodarone, lithium) could indirectly disrupt thyroid function through drug-drug interactions or shared metabolic pathways.[22] Second, patients with preexisting thyroid disorders (eg, autoimmune thyroiditis) may experience exacerbation of thyroid dysfunction due to chemotherapy-induced alterations in immune status, which could unmask or amplify underlying thyroid abnormalities.[23] Third, inter-individual variability in responses to DOX leads to thyroid injury occurring primarily in specific subpopulations (eg, patients receiving long-term high-dose DOX or with comorbid thyroid disorders), whereas insufficient sample sizes restrict the statistical significance of these findings.[24] These factors collectively highlight the complexity of attributing thyroid dysfunction solely to DOX, emphasizing the need for further mechanistic studies and clinical surveillance to clarify these associations.

Direct toxic effects of DOX on the thyroid gland have not been explicitly recognized as common adverse reactions in existing studies. However, clinical observations suggest that DOX may influence thyroid function through several indirect mechanisms.[25] First, as a cytotoxic agent, DOX eliminates tumor cells while potentially triggering immune system activation;[26] in some patients, this process may lead to immune-related adverse reactions (IRAEs), which could theoretically involve the thyroid gland.[27] Second, DOX may induce bone marrow suppression, gastrointestinal disturbances, and other side effects that impair nutrient absorption and metabolism; prolonged or severe metabolic dysregulation can then indirectly interfere with thyroid hormone synthesis, transport, or biological action.[28,29] Third, given DOX`s prominent cardiotoxicity (with severe cases potentially progressing to cardiac dysfunction), and the reciprocal regulatory relationship between thyroid function and the cardiovascular system, cardiac abnormalities may disrupt thyroid hormone secretion and metabolism via neuroendocrine pathways.[30,31]

Here, we investigate the potential direct toxicity of DOX on thyroid follicular epithelial cells, using complementary in vitro (primary mouse thyroid cells) and in vivo (zebrafish larvae) models.[32,33] By integrating molecular, cellular, and histopathological analyses, this study provides the first systematic evidence that DOX may directly disrupt thyroid function, thereby expanding the spectrum of its recognized off-target toxicities and offering new insights into safer therapeutic management for TNBC patients.

# Experimental Methods

## Materials

Specialized culture medium for primary murine thyroid follicular epithelial cells (MTFE cells) were were purchased from Jining Bio Co., Ltd. (Shanghai, China). Mito-Tracker Red CMXRos (C1049B), the JC-1 mitochondrial membrane potential assay kit (C2006), Hoechst 33342 (C1022), Cell scrapers (701001), 4% paraformaldehyde (BL539A) were all purchased from Beyotime Biotechnology (Shanghai, China). Doxorubicin hydrochloride (Dox) was purchased from Sangon Biotech (Shanghai, China). The mitochondrial hydroxyl radical detection assay kit (AAT-A16055) was purchased from AAT Bioquest (Shanghai, China). 2′,7′-Dichlorofluorescein diacetate (DCFH-DA) was bought from MCE. Dulbecco's Modified Eagle Medium high glucose culture medium and PBS buffer were purchased from Gibco (Thermo Fisher Scientific, Inc). Zebrafish triiodothyronine (T3) ELISA Kit (KT21668), Zebrafish thyroxine (T4) ELISA Kit (KT21669), Zebrafish thyrotropin (TSH) ELISA Kit (KT25130), Zebrafish interleukin 1 beta (IL-1β) ELISA Kit (KT36889), Zebrafish interleukin-10 (IL-10) ELISA Kit (KT56363), Zebrafish interleukin-6 (IL-6) ELISA Kit (KT39581), Zebrafish tumor necrosis factor-α (TNF-α) ELISA Kit (KT36259), Zebrafish malondialdehyde (MDA) ELISA Kit (KT25131) were all procured from Wuhan Mosak Biotechnology Co., Ltd (Wuhan, Hubei, China).

## The Isolation of Primary MTFE Cells

Sterile PBS buffer containing $Ca^{2+}$ and $Mg^{2+}$; 0.25% trypsin-EDTA (optional); Type IV collagenase (1~2 mg/mL); DNase I (10~20 μg/mL, optional, to reduce cell clumps); Fetal bovine serum (FBS); DMEM/F12 medium; 75% ethanol; Iodophor (for disinfecting the dissection table); Trypan blue staining solution (for cell viability assessment). 10 cm cell culture dishes; 1.5 mL centrifuge tubes; Pipettes (1 mL, 200 μL, and 10 μL); Ophthalmic scissors; Forceps; Cell strainers (40~70 μm); Centrifuge.

Cell culture biological safety cabinet (BSC-1500IIA2-X), $CO_2$ cell culture incubator set to 5% $CO_2$ and 37°C, inverted fluorescence microscope (Leica), high-speed refrigerated centrifuge (Multifuge X1R, Thermo Fisher), thermostatic blast drying oven (DHG-9123A). Experimental materials and equipment were obtained as described above, the detailed procedures are listed below:[34–36]

### Mouse Anesthesia and Euthanasia

Anesthetize mice with isoflurane (2%–3% v/v) until unresponsive (approximately 2–3 minutes). Following institutional animal ethics guidelines, euthanize the mice by cervical dislocation and proceed immediately with all subsequent steps on ice using pre-chilled solutions.

### Thyroid Tissue Dissection

Make a midline incision along the neck, carefully separate the muscle layer, and expose the trachea. Locate the thyroid glands (appearing pale pink to brownish-yellow, ~1–2 $mm^3$, situated on each side of the trachea at the level of the 3rd-4th cartilage rings). Using micro-forceps, gently dissect away the surrounding connective tissue and blood vessels to avoid mechanical damage. Transfer the isolated thyroid glands to pre-chilled PBS supplemented with 1% FBS and wash twice to remove residual blood.

### Enzymatic Digestion for Cell Dissociation

Mince the cleaned thyroid tissue into small fragments of approximately 1 $mm^3$ and transfer them to a low-adhesion centrifuge tube. Add 2 mL of a pre-warmed enzyme solution containing collagenase IV (1 mg/mL) and DNase I (0.1 mg/mL). Incubate the tube in a 37°C shaking incubator for 15–20 minutes. To ensure thorough digestion and prevent clumping, gently pipette the mixture up and down every 5 minutes. Terminate the digestion by adding 2 mL of DMEM/F12 medium supplemented with 10% FBS.

### Cell Filtration and Initial Purification

Pass the digested cell mixture through a pre-moistened 70 μm cell strainer. Collect the filtrate and centrifuge at 1000 × g for 5 minutes at 4°C. Discard the supernatant and resuspend the cell pellet in pre-chilled PBS (with 1% FBS). Add 1 mL of 1 × red blood cell lysis buffer to the suspension and incubate at room temperature for 3 minutes to lyse contaminating erythrocytes. Neutralize the lysis reaction by adding 5 mL of PBS. Centrifuge again (1000 × g, 5 minutes, 4°C), discard the supernatant, and resuspend the final cell pellet in complete culture medium for subsequent steps.

### Differential Adhesion for Follicular Epithelial Cell Purification

Seed the cell suspension at a density of $1 \times 10^5$ cells per well into 60 mm culture dishes (optionally pre-coated with 0.1% gelatin). Incubate the dishes in a 37°C, 5% $CO_2$ incubator for 2 hours. After this initial adhesion period, gently aspirate the medium containing the non-adherent cells, which are primarily thyroid follicular epithelial cells, and transfer it to a new culture dish. Add fresh complete medium to the new dish, incubate for 24 hours, and then replace the medium to remove any residual non-adherent cells or debris, thereby obtaining a highly purified population of follicular epithelial cells.

### Quality Control

Morphology: Examine under an inverted microscope (typical epithelial cobblestone-like, adherent growth). Immunofluorescence: Stain with anti-thyroglobulin (Tg), followed by DAPI nuclear counterstaining. Purity is confirmed if >90% of cells are positive for thyroid markers (Figure 1).

## In vitro Cell Culture

MDA-MB-231 triple-negative breast cancer cells (ATCC® HTB-26™) were purchased from the Chinese Academy of Sciences (Shanghai, China). For experimental use, MDA-MB-231 cells were cultivated in DMEM high glucose supplemented with 10% FBS and a penicillin-streptomycin cocktail (100 U/mL penicillin and 0.1 mg/mL streptomycin). Cultivation was performed in a $CO_2$ cell culture incubator under controlled conditions of 37°C and 5% $CO_2$ in a humidified atmosphere. All cell stocks were maintained at low passage (P3-P5) to preserve biological consistency.

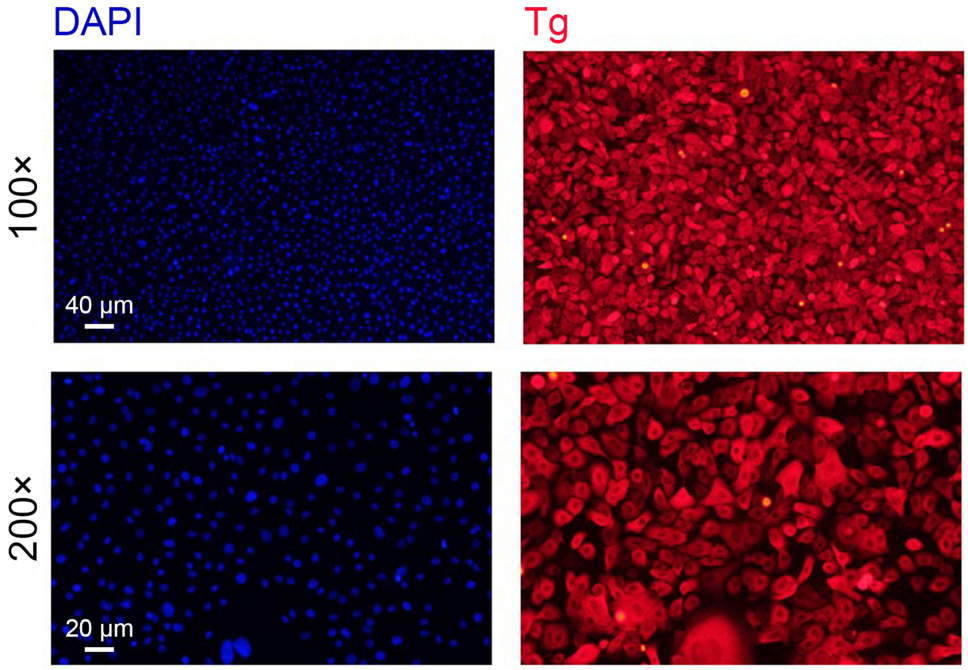


**Figure 1** Identification of Primary MTFE Cells. Scale bar, 40 μm (upper); Scale bar, 20 μm (lower).

Primary MTFE cells were cultured in a manner similar to that described above. It should be noted that specialized culture medium was used for primary cell culture. During primary cell culture, the medium was first replaced after 48 hours, and subsequently changed every 3 days.

Mycoplasma-free status was validated using the MycoAlert mycoplasma detection assay (Lonza, Basel, Switzerland), confirming no detectable mycoplasma contamination.

## Cell Viability

The CCK-8 assay was employed to assess cell viability. The mother liquor of doxorubicin hydrochloride (DOX) was prepared by dissolving it in phosphate buffer to a final concentration of 5 mM (2.9 mg in 1 mL). This stock solution was then serially diluted to obtain working solutions at five concentrations: 100, 200, 300, 400, and 500 nM. MDA-MB-231 and MTFE cells were respectively seeded in 96-well plates at a density of $4 \times 10^4$ cells/well (100 μL/well) and incubated for 24 hours. Subsequently, cells were treated with different concentrations of DOX for varying durations. After discarding the supernatants, the wells were gently washed twice with PBS buffer. Next, 1 mL of serum-free cell culture medium and 100 μL of CCK-8 solution were added to each well, followed by incubation at 37°C for 2~4 hours. Absorbance was measured at 450 nm. All experiments were performed in quintuplicate. Cell viability of the treatment groups was calculated using the following formula:

$$\text{Cell viability } (\%) = \frac{\text{Abs. sample}}{\text{Abs. control}} \times 100$$

## Drug Permeation Test

Transwell culture plates (0.4 μm, Corning) were used in this experiment. MDA-MB-231 cells were cultured in DMEM high-glucose medium at 37°C for 24 hours, then harvested and resuspended in the same medium. The cell suspension was adjusted to a concentration of $3 \times 10^4$ cells/200 μL and added to the upper chamber. DMEM high-glucose medium was added to the lower chamber. At different time points post-incubation, the medium in the lower chamber was collected to measure the fluorescence intensity of DOX efflux using a microplate reader (Bio-Rad, Shanghai, China).


https://doi.org/10.2147/DDDT.S576622

## In vitro Cellular Uptake Experiments

The same experimental procedure used for seeding MDA-MB-231 cells onto the upper chamber as described above was applied. Additionally, MTFE cells were cultured in specialized medium at 37°C for 24 hours, harvested, and resuspended in the same medium. Next, MTFE cells were condensed to $3\times10^4$ cells in 200 μL cell suspension and then added to the cell climbing slices which were placed in the lower chamber. After 24 hours of culture, both cell types showed adherent growth, and their viability was suitable for the cellular uptake assay. DOX solutions of varying concentrations were prepared in serum-free DMEM high-glucose medium and added to the upper chamber. Following 72 hours of treatment, the cell climbing slices were taken out for visualization via confocal microscopy using an A1 Plus confocal system (Nikon Instruments).

## Flow Cytometry Assay

The cellular uptake behaviors of the DOX in MTFE cells were analyzed using flow cytometry (BD biosciences). For flow cytometry analyses, MTFE cells seeded on cell climbing slices in the lower chamber of the transwell insert were washed with PBS after trypsin digestion. After centrifugation and washing with PBS, red fluorescence of DOX was analyzed by flow cytometry, and data were analyzed using FlowJo (Tree Star). The data obtained from flow cytometry are displayed as a single-parameter histogram, where the y-axis represents the number of cells (generally relative count) corresponding to a specific fluorescence intensity on the x-axis. In this histogram, a rightward shift of the peak indicates a higher fluorescence intensity.

## Intracellular ROS Assay

MTFE cells were incubated with 300 nM DOX at 37°C for 30 min in the dark (within a 72-hour experimental period). Subsequently, the plates were washed three times with PBS buffer. The DCFH-DA stain detecting ROS production was observed using a fluorescence microscope (Nikon, Japan).

## The Detection of Mitochondrial ROS Levels

Mitochondrial ROS levels were assessed using the mitochondrial superoxide-specific fluorescent probe MitoSOX Red. Following experimental treatment, MTFE cells seeded in confocal microscopy dishes were incubated with 5 μM Mito-Tracker Red CMXRos at 37°C for 30 minutes. Post-staining, cells were thoroughly rinsed with PBS buffer and maintained in a live-cell imaging medium supplemented with 25 mM glucose to preserve viability. Confocal imaging was conducted using an A1 Plus confocal laser scanning microscope (Nikon Instruments). Fluorescence intensity of MitoSOX Red was quantified in a minimum of 100 cells distributed across 10 randomly selected microscopic fields. Quantitative analysis of the acquired images was performed with ImageJ software.

## Analysis of Mitochondrial Morphology and Mitochondrial Membrane Potential

Alterations in mitochondrial morphology were evaluated using MitoTracker Red (Beyotime). Post-treatment, cells were gently rinsed with phosphate-buffered saline (PBS) and subsequently incubated with 100 nmol/L MitoTracker Red at 37°C for 20 minutes to allow probe uptake. Mitochondrial structural dynamics were visualized via confocal laser-scanning microscopy (CLSM). Mitochondrial membrane potential ($\Delta\Psi m$) was assessed using a JC-1 Mitochondrial Membrane Potential Assay Kit (Beyotime), with fluorescence signals captured using CLSM. Quantitative analysis of fluorescence intensity was performed using ImageJ software (National Institutes of Health) to determine morphological and functional changes.

## Establishment of Zebrafish Model

Wild-type AB strain zebrafish (Danio rerio) were obtained from the China Zebrafish Resource Center (Wuhan, China) and maintained in a recirculating aquaculture system at 28.5°C (pH 7.2–7.5) under a 14-hour light/10-hour dark cycle. Feeding was initiated at 4 days post-fertilization (dpf) using paramecia and Artemia nauplii. At 4 dpf, larvae were exposed to 20 μM DOX via static immersion in embryo medium[37] The treatment lasted for 48 hours, with the medium being renewed daily to maintain drug stability. Six biological replicates of 30 embryos each were analyzed in each group.

## ELISA Tests

Wild-type AB zebrafish larvae at 4 days post-fertilization (dpf) were randomly assigned to experimental groups and cultured in 6-well plates, with 30 individuals per well across all groups. After treatment, a defined volume of PBS (pH 7.4) was added to each well. Samples were promptly frozen in liquid nitrogen for short-term storage, then thawed and maintained at 2~8°C. Subsequently, a specified volume of PBS (pH 7.4) was introduced, and tissues were homogenized thoroughly using either manual disruption or a mechanical homogenizer. Homogenates were centrifuged at 2000~3000 × g for approximately 20 minutes, and supernatants were carefully collected. Total protein concentration was measured using the Bradford assay with bovine serum albumin (BSA) as a standard. For each sample, cytokine concentrations were divided by the total protein concentration to obtain a normalized cytokine level. Concentrations of MDA, IL-1β, TNF-α, IL-6, IL-10, T4, TSH, T3, and TRH in zebrafish samples were quantified via enzyme-linked immunosorbent assay (ELISA) kits, with six replicates per treatment group. Data acquisition and statistical analysis were performed subsequently.

## TEM and Pathological Section Analysis

To conduct electron microscopic characterization, 4 dpf zebrafish larvae were immobilized using a dual-fixative solution comprising 2% paraformaldehyde and 0.2% glutaraldehyde in 0.1 M PBS. Post-fixation, specimens were processed through PBS-glycine washing to eliminate unreacted aldehydes, followed by sequential embedding in gelatin and infiltration with 2.3 M sucrose. Ultrathin sections (50-nm thickness) were made at −120°C using an Ultracut-S ultramicrotome (Leica Microsystems) and immediately visualized under the TEM (TecnaiG2 spirit Biotwin; FEI).

Subsequent to larval sample preparation, histological sections were fabricated. Sections were mounted onto glass slides and air-dried to stabilize. Paraffin embedding material was then removed via standard dewaxing procedures, followed by distilled water rinsing. Hematoxylin staining was applied for a defined duration, after which sections underwent dehydration through graded alcohols (70% and 90%) for 10 minutes. Eosin counterstaining was performed for 2~3 minutes to enhance cytoplasmic contrast. Finally, tissue architecture was scanned using a Leica SCN400 slide scanner, and morphological data were systematically analyzed to characterize structural features.

## Data and Statistical Analysis

Quantitative results are reported as mean ± standard deviation (SD). Statistical evaluations were carried out using Graphpad Prism version 10.1.2. Pairwise group comparisons were assessed via Student's *t*-test, while multi-group differences were analyzed through one-way analysis of variance (ANOVA). A significance threshold of $P < 0.05$ was established for all analyses.

# Results and Discussion

## Cytotoxicity Test to Evaluate in vitro Antitumor Activity of DOX

To evaluate the anti-tumor efficacy of DOX in TNBC, we selected the MDA-MB-231 cell line for the in vitro CCK assay. MDA-MB-231 cells were exposed to varying concentrations of DOX (100 nM, 200 nM, 300 nM, 400 nM, 500 nM) for two time points: 24 hours and 48 hours. As shown in Figure 2a and b, at low concentrations (≤200 nM), DOX treatment did not induce significant proliferative inhibition in MDA-MB-231 cells, regardless of the incubation duration (24 or 48 hours). In contrast, when the concentration was increased to 300 nM, a marked reduction in cell viability was observed after 24 hours of treatment, with viability dropping to less than 60% compared to the untreated control group. Particularly, extending the incubation time to 48 hours did not further enhance the cytotoxic effect (Figure 2c). Further analysis revealed a clear concentration-dependent relationship, as DOX concentrations increased from 100 nM to 500 nM, cell viability decreased progressively.

Collectively, these data confirm the expected antitumor activity of DOX in TNBC cells. A concentration of 300 nM for 24 h was identified as the minimum effective condition for significant growth inhibition, which provided a reference point for subsequent toxicity studies. These findings not only validate DOX as an effective therapeutic agent for TNBC but also provide critical parameters (300 nM, 24 hours) to guide the design of subsequent preclinical studies.

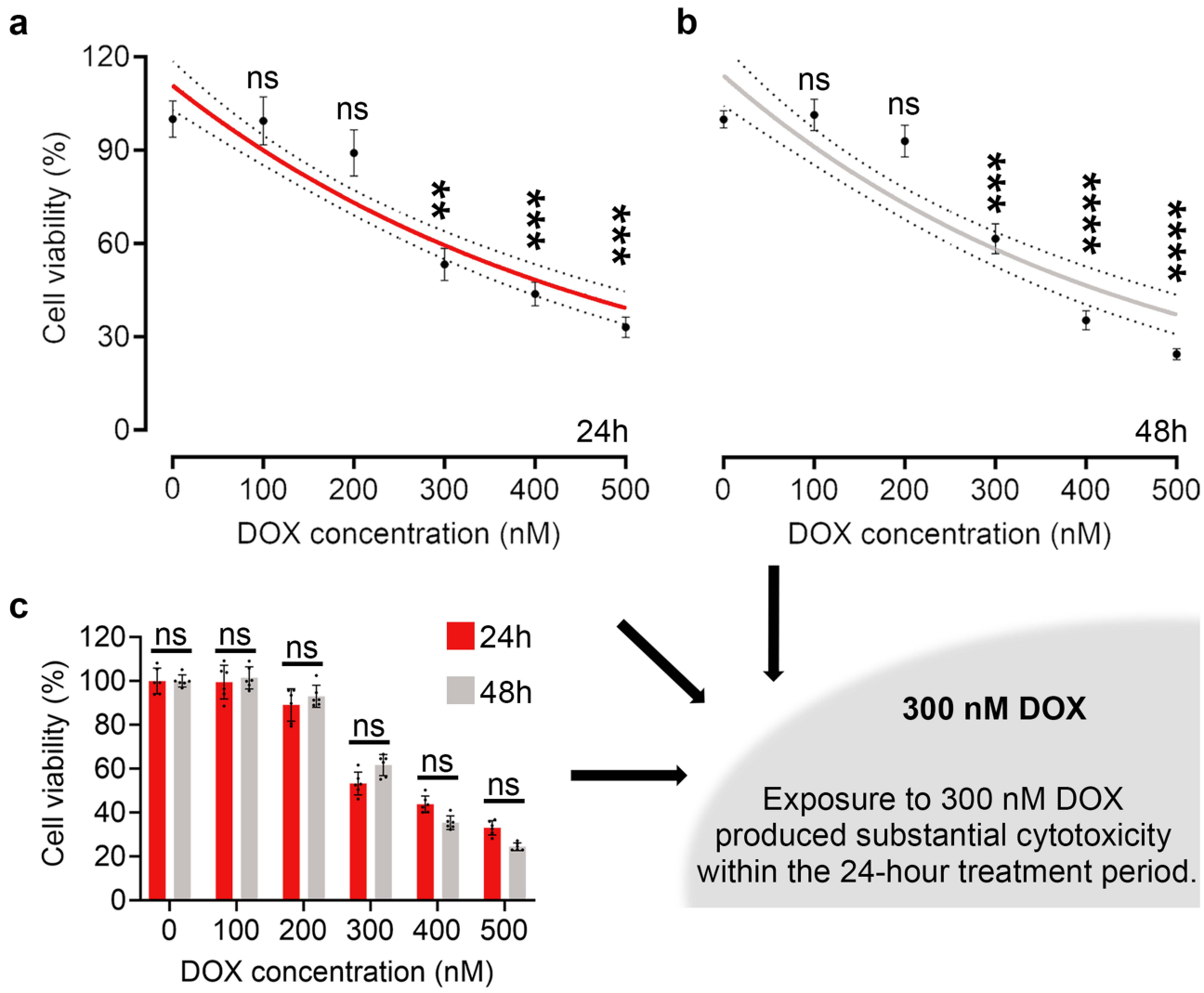


**Figure 2** Screening of chemotherapeutic drug cytotoxicity of DOX in vitro TNBC models. (**a**) Cytotoxicity of DOX at different concentrations on MDA-MB-231 cells for 24 h. Data were presented as mean ± SD (n = 6; ns, no significant difference vs 0 nm (DOX concentration); ***p* < 0.01 vs 0 nm (DOX concentration); ****p* < 0.001 vs 0 nm (DOX concentration); one-way ANOVA + Tukey`s multiple comparisons test). (**b**) Cytotoxicity of DOX at different concentrations on MDA-MB-231 cells for 48 h. Data were presented as mean ± SD (n = 6; ns, no significant difference vs 0 nm (DOX concentration); \*\*\**p* < 0.001 vs 0 nm (DOX concentration); \*\*\*\**p* < 0.0001 vs 0 nm (DOX concentration); one-way ANOVA + Tukey`s multiple comparisons test). (**c**) Comparison of DOX-induced inhibition of MDA-MB-231 cell proliferation at 24 h vs 48 h. Data were presented as mean ± SD (n = 6; ns, no significant difference vs control group (24 h); two-factor ANOVA with + Tukey`s multiple comparisons test).

## Cellular Efflux of DOX

Dox efflux assays were performed to test whether strong DOX efflux properties correlated with increased DOX concentrations and longer incubation times. To investigate the efflux behavior of DOX in MDA-MB-231 cells, we employed a transwell assay. MDA-MB-231 cells were seeded in the upper chamber, which was designed to allow permeation of a small-molecule drug such as DOX. Following treatment, DOX that had effluxed from the upper chamber and permeated into the lower chamber was collected. The concentration of DOX in the lower chamber was then quantitatively measured using a fluorometric microplate reader, as shown in Figure 3a.

Through in vitro experiments, it was observed that the amount of DOX effluxed from cells incubated with DOX did not increase over time when the DOX concentrations were ≤ 200 nM. Meanwhile, when the DOX concentration reached and exceeded 300 nM, the amount of DOX effluxed from cells exhibited an upward trend over time (Figure 3b). Further data analysis revealed that when the DOX concentration exceeded 200 nM and the incubation time with MDA-MB-231 cells surpassed 24 hours, the amount of DOX effluxed from the cells displayed a significant upward trend. Importantly, this trend continued to escalate with both prolonged incubation time and increasing DOX concentrations (Figure 3c).

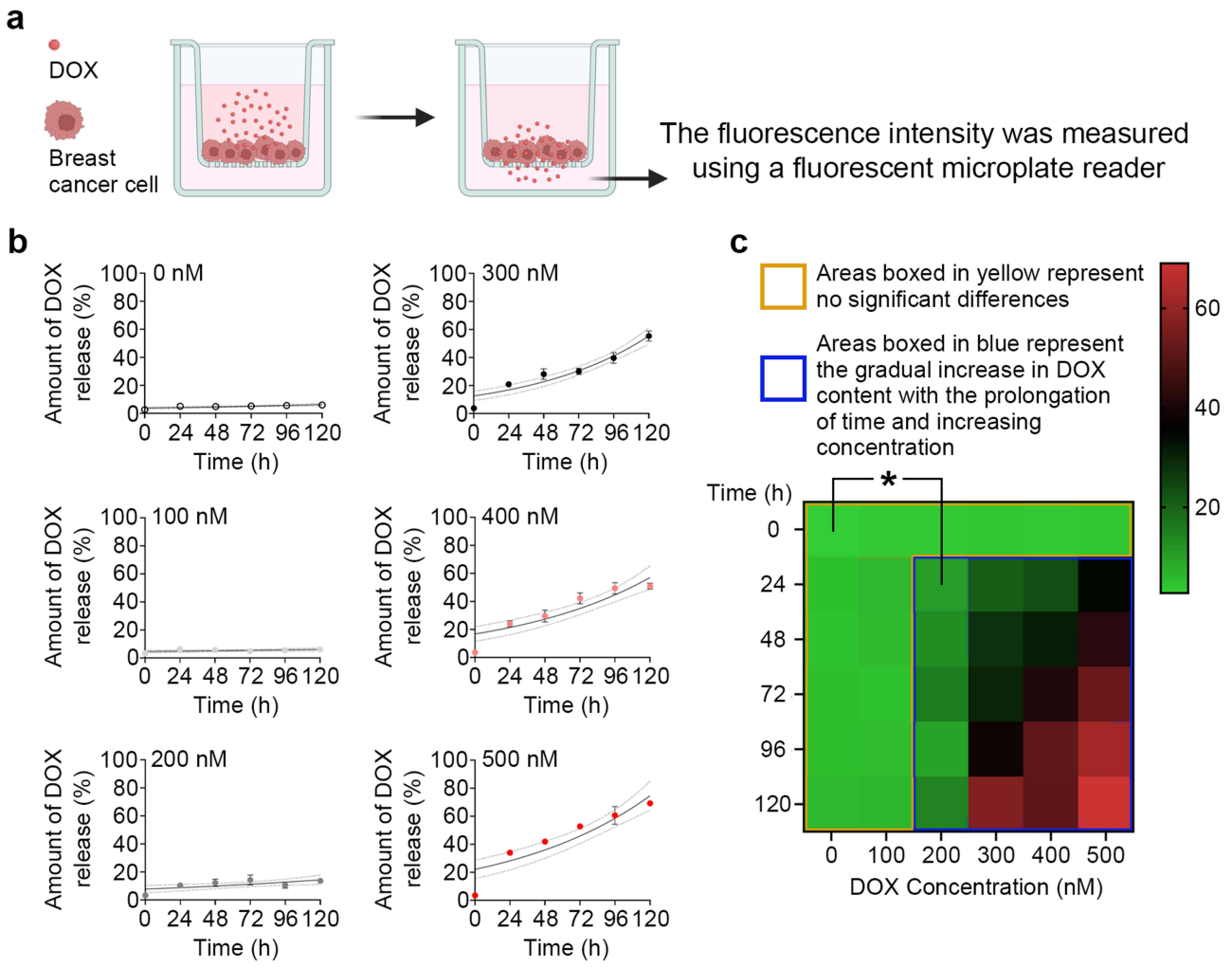


**Figure 3** In vitro assay for studying DOX efflux (**a**) Schematic representation of transwell assay. (**b**) Cumulative efflux amount of DOX at different concentrations over 120 h. (**c**) Analysis and comparison of DOX efflux amounts at varying concentrations over 120 h. Data were presented as mean ± SD (n = 6; *$p$ < 0.05 vs 0 nm (DOX concentration) at 0 h; two-factor ANOVA with + Tukey`s multiple comparisons test).

DOX exerts anti-tumor activity via DNA intercalation and topoisomerase II inhibition; however, its clinical utility is often compromised by multidrug resistance (MDR), a key mechanism linked to enhanced drug efflux from tumor cells.[38] Mechanistically, enhanced efflux at supratherapeutic doses was associated with upregulated expression of ATP-binding cassette (ABC) transporters, including P-glycoprotein (P-gp/ABCB1) and multidrug resistance-associated protein 1 (MRP1/ABCC1)-key mediators of drug extrusion in MDR.[39–41] These transporters utilize ATP hydrolysis to actively pump DOX out of cells, reducing intracellular drug levels and cytotoxicity.[42] Enhanced efflux of DOX at higher concentrations was consistent with upregulation of multidrug resistance transporters.[43] While this phenomenon reduces intracellular drug accumulation in tumor cells, it may also increase extracellular DOX exposure, raising the possibility of off-target toxicity in non-malignant cells.

## Effects of Effluxed DOX on MTFE Cells

To simulate the impact of DOX efflux on normal thyroid tissue during TNBC treatment, we isolated primary MTFE cells and used a transwell assay to model this process. As shown in Figure 4a, MDA-MB-231 cells seeded in the upper chamber were treated with DOX, and the effluxed free DOX diffused into the lower chamber, where it interacted with the MTFE cells. The results from our study (Figure 4b) showed that when tumor cells were exposed to DOX at concentrations ≤ 200 nM, the effluxed DOX that reached the lower chamber caused no significant damage to the MTFE cells


https://doi.org/10.2147/DDDT.S576622

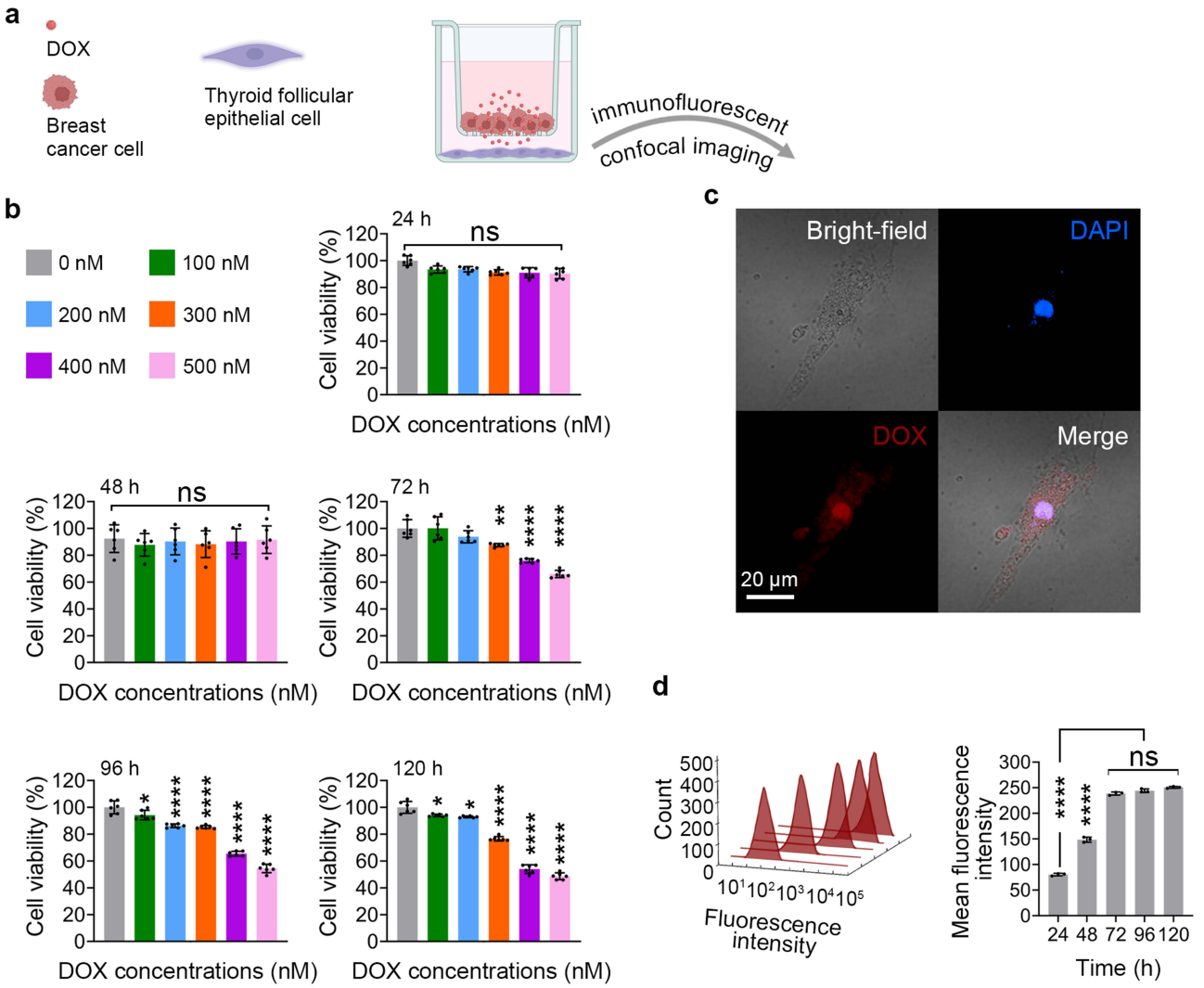


**Figure 4** Cellular uptake studies on free DOX in the MTFE cells. (**a**) Schematic diagram of transwell permeability assay. (**b**) Measurements of cell viability at different DOX concentrations over different exposure times. Data were presented as mean ± SD (n = 6; ns, no significant difference vs 0 nm (DOX concentration); *$p$ < 0.05 vs 0 nm (DOX concentration); **$p$ < 0.01 vs 0 nm (DOX concentration); ****$p$ < 0.0001 vs 0 nm (DOX concentration); one-way ANOVA + Tukey`s multiple comparisons test). (**c**) Confocal imaging of DOX cellular uptake in MTFE Cells. Scale bar, 20 μm. (**d**), Flow cytometry analysis of DOX uptake. Data were presented as mean ± SD (n = 6; ns, no significant difference vs 72 h; ****$p$ < 0.0001 vs 24 h; one-way ANOVA + Tukey`s multiple comparisons test).

within the first 72 h. However, after 96 h of exposure, cytotoxicity became evident. Notably, at a higher DOX concentration (300 nM), the cumulative amount of effluxed DOX in the lower chamber induced significant damage to MTFE cells as early as 72 hours after treatment. Furthermore, the cell damage was further aggravated by the extension of the experimental time and the concentration of DOX.

These findings suggest that prolonged exposure to effluxed DOX, even at relatively low concentration (≤ 200 nM), may eventually compromise thyroid cells viability, whereas higher concentrations (≥ 300 nM) accelerate this process in a dose- and time-dependent manner. This dose- and time-dependent pattern highlights the importance of considering potential off-target effects of DOX beyond tumor cells, reinforcing the need to evaluate its impact on non-malignant tissues with high metabolic activity, such as the thyroid.

To further authenticate the findings, the cellular uptake of DOX was investigated in MTFE cells by CLSM and flow cytometry. Based on our prior toxicological investigations, we selected a DOX concentration of 300 nM and a 72-hour incubation period. Subsequent confocal microscopy analysis revealed that red-fluorescent DOX had successfully penetrated into MTFE cells, with clear intracellular localization observed (Figure 4c). Besides, the cellular uptake of DOX (300 nM) was further confirmed by flow cytometry (Figure 4d), analysis showed that the amount of DOX taken up


https://doi.org/10.2147/DDDT.S576622

by the MTFE cells is closely associated with the time of drug action, the stronger the fluorescence and the longer the incubation time. After 72 hours, no significant differences in the MTFE cells taken between groups were observed.

## DOX-Induced Oxidative Stress Injury in MTFE Cells

Several studies have reported that DOX leads to oxidative stress, induces significant toxicities in normal tissues during cancer treatment, primarily driven by excessive ROS generation.[44] DOX enters cells and complexes with free iron ions, catalyzing the Fenton reaction to produce high levels of superoxide anions ($O_2^-$) and hydroxyl radicals ($^{\cdot}OH$), reactive molecules that damage cellular lipids, proteins, and DNA, ultimately triggering dysfunction and apoptosis.[45] Concurrently, DOX disrupts redox homeostasis by suppressing antioxidant enzymes (eg, superoxide dismutase (SOD), glutathione peroxidase (GPx)) and depleting endogenous antioxidants like glutathione (GSH), impairing the cell's capacity to neutralize ROS and exacerbating oxidative stress.[46]

To evaluate DOX-induced oxidative damage in normal thyroid tissue, we focused on MTFE cells, critical for thyroid hormone synthesis. Using DCFH-DA for intracellular ROS detection, we observed a marked increase in green fluorescence intensity in DOX-treated MTFE cells compared to controls, indicating a significant rise in ROS levels (Figure 5a and c). Given the high metabolic demand of thyroid follicular cells, which rely on mitochondria for ATP production, we further assessed mitochondrial integrity using a fluorometric one-step mitochondrial hydroxyl radical detection assay kit. Confocal microscopy revealed intensified red fluorescence in DOX-exposed cells, corresponding to elevated mitochondrial $^{\cdot}OH$ accumulation (Figure 5b). Quantitative analysis confirmed a 2-fold increase in mitochondrial hydroxyl radical damage in DOX-treated groups versus controls (Figure 5d). These results support a model in which oxidative stress, mediated by excessive ROS generation and impaired antioxidant defense, contributes to DOX-induced injury in MTFE cell.

## Effect of DOX on Mitochondria of MTFE Cells

Building on our prior findings that DOX induces mitochondrial oxidative stress in normal MTFE cells via ROS, we further characterized its toxicological impact on mitochondrial structure and functions. Emerging evidence from breast cancer studies highlights that DOX disrupts mitochondrial morphology and function in cardiomyocytes, with such abnormalities closely correlating to impaired cardiac performance. Given the central role of MTFE cells in maintaining thyroid homeostasis, investigating whether DOX induces comparable mitochondrial alterations in these cells is of significant relevance.

Using Mitotracker fluorescent staining and confocal microscopy, we observed distinct morphological changes in DOX-treated MTFE cells. Normal cells without DOX treatment displayed uniform, filamentous mitochondrial distribution, DOX exposure rapidly induced mitochondrial condensation and nuclear clustering (Figure 6a and c), consistent with early stress-induced fission-fusion dysregulation. Mitochondrial membrane potential (MMP), a key health indicator, was assessed via JC-1 staining. Quantitative analysis revealed a 5-fold increase in green-to-red fluorescence intensity in DOX-treated cells, confirming significant MMP collapse (Figure 6b and d). Loss of mitochondrial membrane potential (MMP) is a hallmark of mitochondrial dysfunction and apoptosis, disrupting electron transport, reducing ATP production, and activating pro-apoptotic pathways. Such alterations in thyroid follicular cells may impair hormone synthesis, providing a mechanistic link between DOX exposure and thyroid dysfunction. Together, these findings provide experimental evidence that DOX can directly impair thyroid cell function through oxidative stress and mitochondrial disruption. This expands the spectrum of recognized DOX toxicities and highlights the need for thyroid function monitoring in clinical settings.

## Evaluation of DOX Biosafety During Zebrafish Development

Zebrafish (Danio rerio) are increasingly used as a vertebrate model to evaluate the safety and toxicity of drugs in vivo.[47] Leveraging these advantages, we investigated the effects of DOX on inflammatory responses and thyroid function in zebrafish larvae to provide a comprehensive assessment of its systemic toxicities (Figure 7a). Oxidative stress, a major cause of organ damage, was measured using malondialdehyde (MDA); ELISA revealed significantly elevated MDA levels in DOX-treated larvae, consistent with DOX-induced oxidative stress injury (Figure 7b). Inflammation was

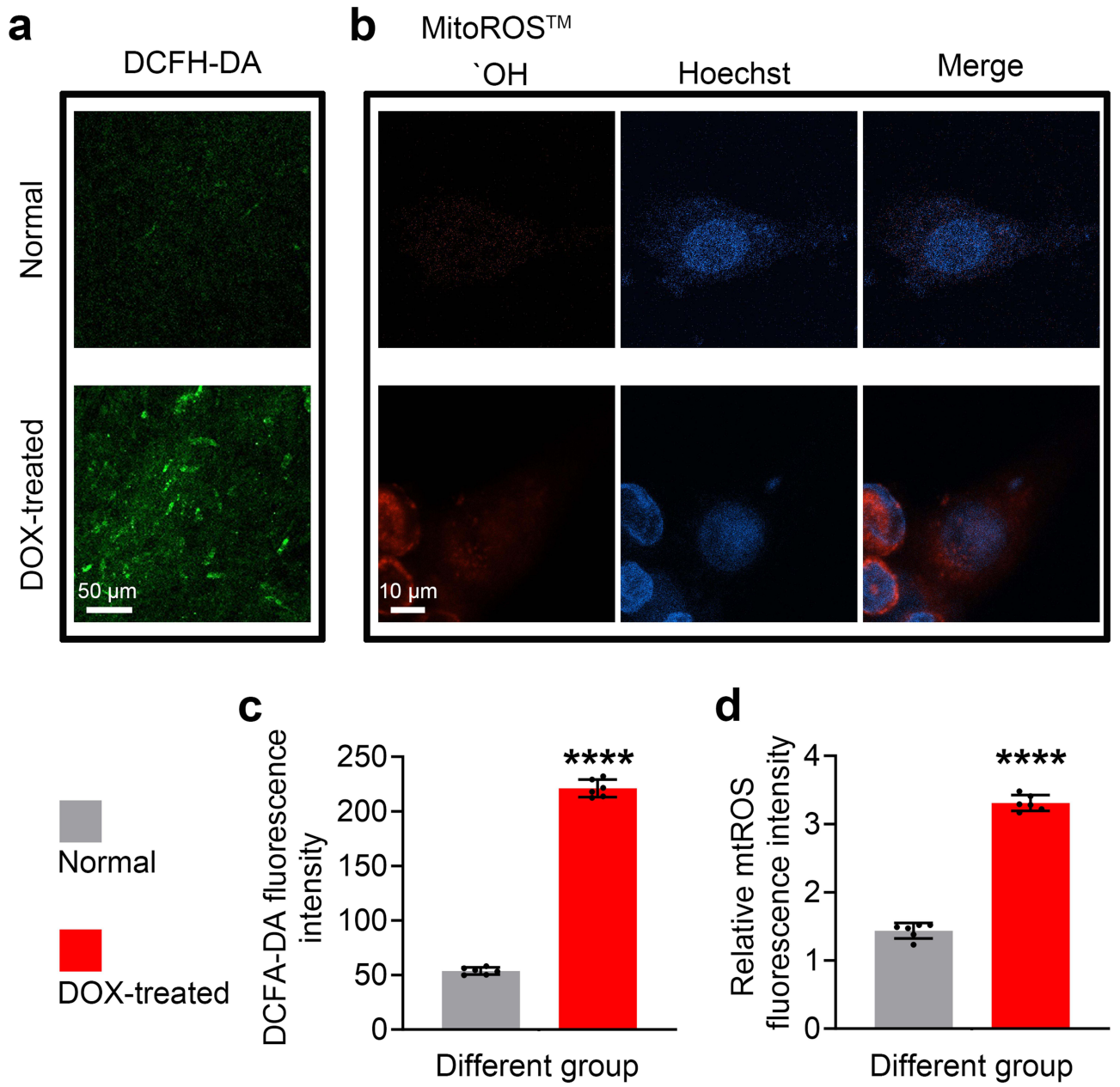


**Figure 5** Oxidative damage induced by DOX in MTFE cells. (**a**) Confocal microscopy images of cellular ROS. Scale bar, 50 μm. (**b**) Confocal microscopy analyses of mitochondrial oxidative stress after DOX treatment. Scale bar, 10 μm. (**c**) Quantification of DCFH-DA fluorescence intensity in MTFE cells. (**d**) Statistical analysis of fluorescence intensity of mitochondrial oxidative stress in MTFE cells. Data were presented as mean ± SD (n = 6; ****$p < 0.0001$ vs normal group; Unpaired *t*-test).

assessed via cytokine profiling: DOX upregulated pro-inflammatory factors TNF-α and IL-1β but did not alter anti-inflammatory IL-10 or pro-inflammatory IL-6 levels, indicating selective activation of the TNF-α/IL-1β axis without compensatory anti-inflammatory responses (Figure 7c–f). Meanwhile, ELISA showed significant increases in T3 and T4 levels alongside decreased TSH and TRH (key regulators of the hypothalamic-pituitary-thyroid (HPT) axis) in DOX-treated larvae (Figure 7g–j), suggesting impaired thyroid hormone (TH) synthesis and disrupted negative feedback regulation of the HPT axis.

Collectively, these data demonstrate that DOX induces multisystem toxicity in zebrafish larvae, characterized by oxidative stress, inflammatory dysregulation, and thyroid hormone imbalance. Oxidative stress likely acts as a primary trigger, driving inflammation via TNF-α/IL-1β activation and impairing thyroid function through suppression of the HPT axis. In vivo data from zebrafish larvae revealed that DOX exposure was associated with oxidative stress, selective pro-

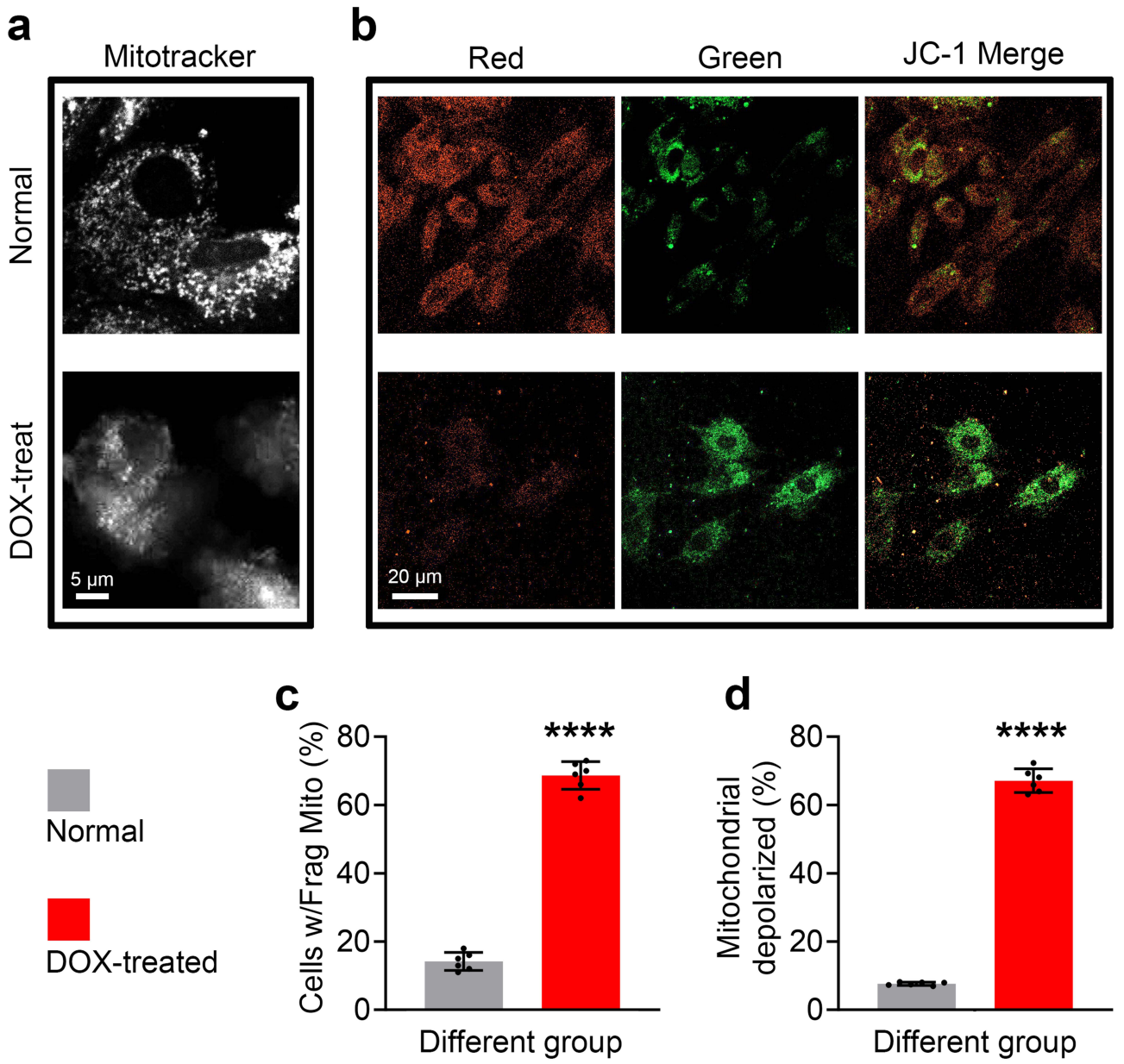


**Figure 6** DOX induces structural and functional abnormalities in mitochondria. (**a**) The morphological features of mitochondria were observed under CLSM. Scale bar, 5 μm. (**b**) The mitochondrial membrane potential was detected by JC-1 staining. Scale bar, 20 μm. (**c**) The objective quantification of mitochondrial morphology in MTFE cells. (**d**) Quantification of the mitochondrial polarization. Data were presented as mean ± SD (n = 6; ****$p < 0.0001$ vs normal group; Unpaired *t*-test).

inflammatory activation, and alterations in thyroid hormone levels, consistent with impaired regulation of the hypothalamic–pituitary–thyroid axis.

## Observation of Mitochondrial Morphology

The structural integrity and ultrastructural morphology of mitochondria are tightly linked to cell viability; morphological abnormalities often signal functional impairment or even severe cellular damage.[48,49] To evaluate mitochondrial changes in DOX-treated zebrafish larvae thyroid tissues, we used TEM, a high-resolution technique for visualizing subcellular architecture. In the normal group with DOX treatment, healthy mitochondria showed typical features: a double-membraned, vesicular or elongated structure with inner membranes invaginated into variably shaped cristae, whose cross-sections appeared as linear profiles under TEM (Figure 7a). In contrast, unhealthy mitochondria displayed


https://doi.org/10.2147/DDDT.S576622

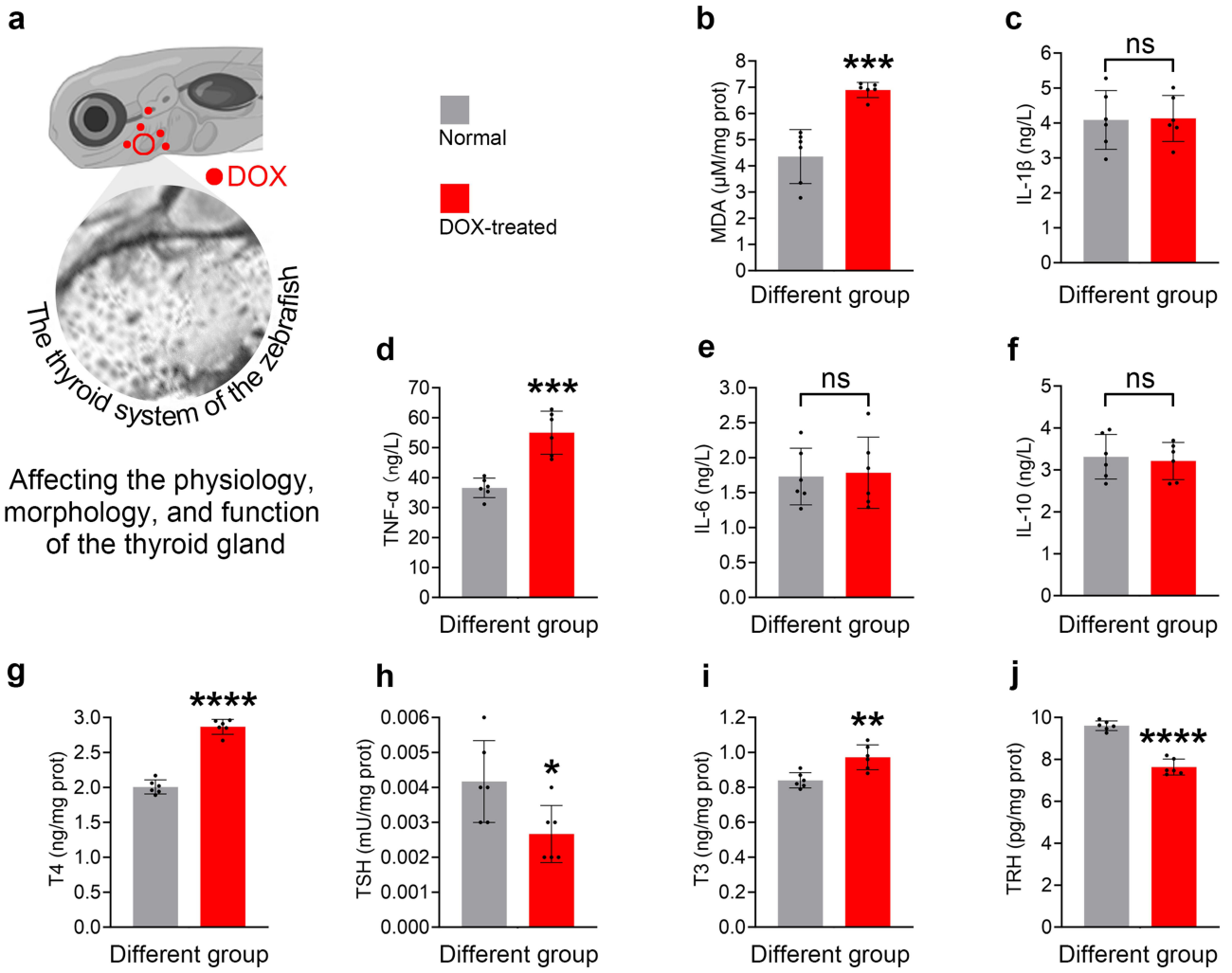


**Figure 7** Evaluation of the cytotoxic effect of DOX was carried out using a zebrafish model. (**a**) Schematic diagram of the anatomical structure of the thyroid gland in zebrafish larvae. (**b–j**) ELISA analysis of MDA (**b**), IL-1β (**c**), TNF-α (**d**), IL-6 (**e**), IL-10 (**f**), T4 (**g**), TSH (**h**), T3 (**i**) and TRH (**j**). Data were presented as mean ± SD (n = 6; ns, no significant difference vs normal group; *$p < 0.05$ vs normal group; **$p < 0.01$ vs normal group; ***$p < 0.0001$ vs normal group; ****$p < 0.0001$ vs normal group; Unpaired *t*-test).

pathological signs, including matrix swelling, expanded intercristal spaces, condensation, cristae disintegration or loss, and eventual irreversible necrosis. Indeed, TEM analysis revealed DOX-induced mitochondrial damage characterized by prominent alterations such as matrix enlargement, shortened and sparse cristae, and severe swelling, all of which signal significant structural disorganization (Figure 8a).

To systematically quantify DOX-induced thyroid injury, we categorized mitochondrial morphological changes into five grades based on ultrastructural criteria: Grade I: intact membrane, distinct cristae, and uniform electron density; Grade II: disordered, indistinct cristae; Grade III: partial mitochondrial swelling; Grade IV: matrix vacuolation with multiple electron-lucent areas; Grade V: near-complete cristae loss, condensed morphology, and autophagic lysosome accumulation.[50,51] Quantitative analysis showed a marked reduction in the proportion of Grade I mitochondria in DOX-treated groups versus controls. Meanwhile, Grades II and III increased significantly (Figure 8b). Overall, ultrastructural observations indicated that DOX exposure was associated with mitochondrial swelling, cristae disintegration, and loss of integrity in thyroid follicular cells, changes that may reflect activation of stress pathways such as ferroptosis or mitophagy.

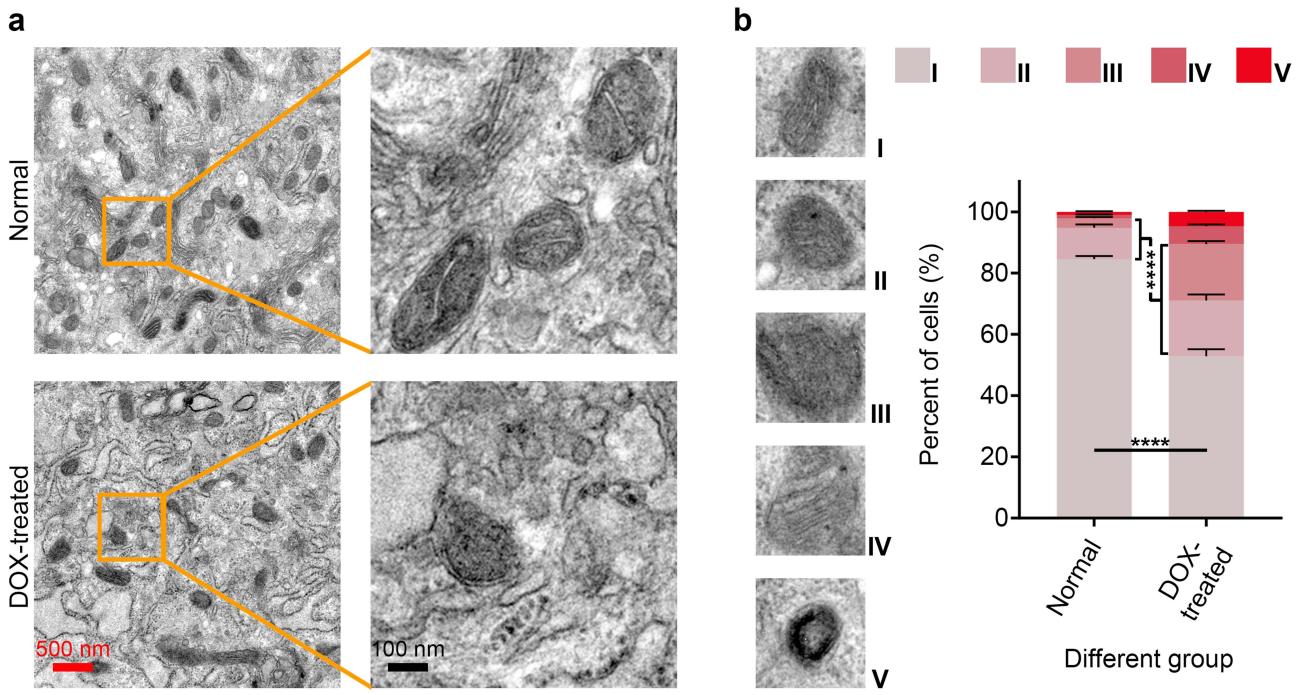


**Figure 8** Observations of mitochondrial ultrastructure. (**a**) Representative TEM pictures of mitochondria. Scale bar (red), 500 nm; Scale bar (Orange), 100 nm. (**b**) Ultrastructural comparative analysis. Data were presented as mean ± SD (n=3 replicates per group; For each group, 20 cells were counted; ****$p < 0.0001$ vs normal group; two-factor ANOVA with + Tukey`s multiple comparisons test).

## Pathological Section Analysis

H&E and Masson`s trichrome staining were used to further confirm the injurious effects of DOX on the thyroid gland of zebrafish larvae (Figure 9). H&E staining results revealed that in the control group, the thyroid follicular epithelial cells of zebrafish larvae exhibited a regular cuboidal or low columnar shape, arranged neatly and closely around the follicular lumen. The nuclei were uniform in morphology, and the colloid within the lumen appeared as a homogeneous deep red stain due to its strong eosinophilia. In contrast, the DOX-treated group exhibited significant abnormalities, the follicular epithelial cells were disorganized, loosely arranged, overlapping, and even detached from the basement membrane. The nuclei showed a significantly increased incidence of pyknosis, karyorrhexis, and karyolysis, indicating the activation of apoptotic or necrotic processes. The cytoplasm contained numerous vacuoles of varying sizes, which were speculated to be associated with mitochondrial damage and oxidative stress-induced lipid peroxidation and organelle disintegration. Furthermore, the follicular lumina were dilated to varying degrees, with a reduction in colloid or the appearance of vacuolation. The normally strongly eosinophilic red-stained colloid appeared heterogeneously pale or vacuolated, with blurred boundaries, reflecting colloid protein denaturation, likely due to reduced secretion or oxidative degradation.

Masson trichrome staining results further revealed remodeling of the extracellular matrix. In normal thyroid tissue, collagen fibers in the interstitium were minimal, distributed only perivascularly and within the interfollicular connective tissue. In the DOX-treated group, however, interstitial collagen deposition was significantly increased, with expanded areas of blue collagen fibers between follicles, indicating the activation of fibroblasts and initiation of a repair response involving collagen secretion, demonstrating an early fibrotic tendency. Histopathological analysis with H&E and Masson`s trichrome staining showed disorganization of follicular epithelium, nuclear changes consistent with cell death, and increased interstitial collagen deposition. These findings suggest early tissue remodeling in response to DOX exposure.

DOX remains a cornerstone chemotherapy for TNBC due to the lack of targeted therapies, yet its use is increasingly associated with thyroid dysfunction-a significant but underexplored off-target effect. Our findings demonstrate that DOX induces direct thyroid cell injury, characterized by oxidative stress and inflammatory activation, mirroring the clinical vulnerability of TNBC patients to endocrine toxicity. This aligns with growing


https://doi.org/10.2147/DDDT.S576622

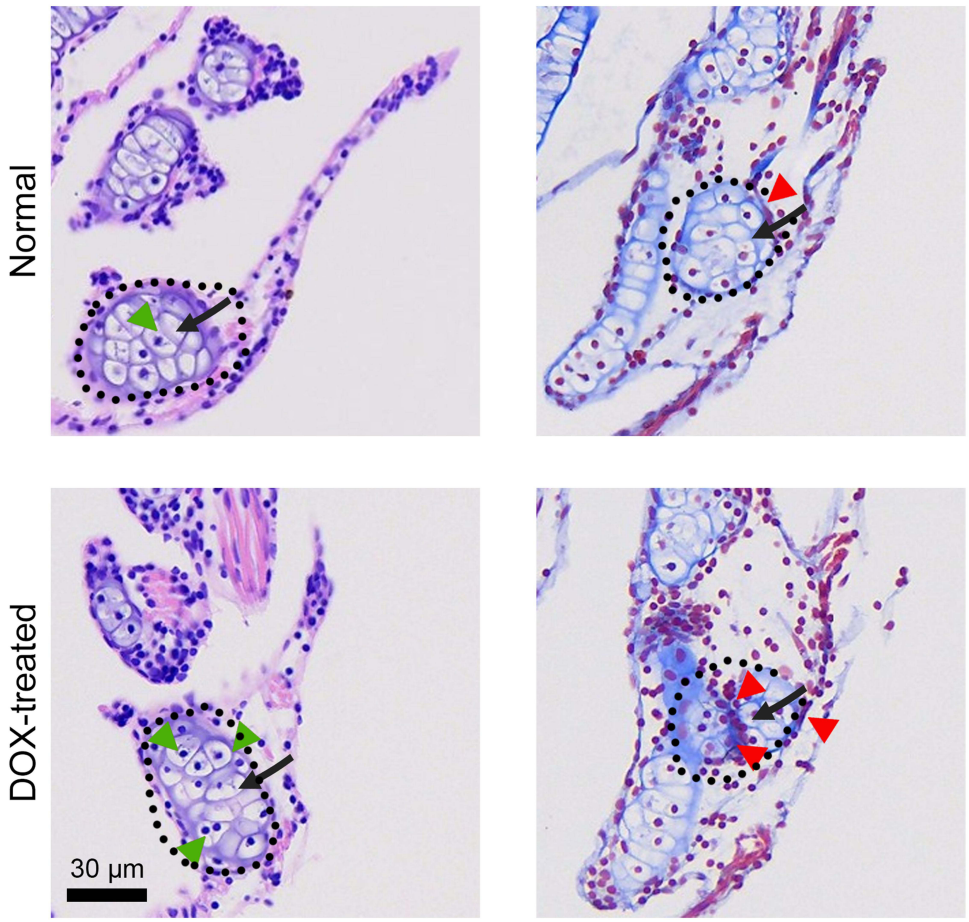


**Figure 9** Representative H&E-stained and Masson trichrome-stained thyroid tissue sections. Scale bar, 30 μm. Black dashed lines represent thyroid tissue; Black arrows indicate the thyroid follicles; The green arrows indicate the inflammatory cell infiltration; The red arrows indicate collagen deposition.

preclinical evidence underscoring DOX-induced thyroid damage. Specifically, Babalola et al (2025) identified oxidative stress as a key mediator in DOX-provoked thyroid dysfunction, while ALHOWAIL (2023) reported DOX-mediated hypothyroidism alongside cardiotoxicity, further confirming thyroid hormone dysregulation. Additionally, Alotayk et al (2023) linked DOX to systemic inflammatory responses and hypothyroidism, supporting the notion that thyroid injury is part of DOX`s broader toxicological profile.[52–54] Collectively, these studies establish a consistent phenotype of DOX-driven thyroid impairment, primarily mediated by oxidative and inflammatory pathways. By modeling DOX-thyroid interactions in a TNBC context, our work not only reinforces the clinical plausibility of this side effect but also emphasizes the need for proactive thyroid monitoring in this high-risk patient population. These insights contribute to a mechanistic framework for understanding how systemic chemotherapy propagates toxicity to endocrine organs and may inform future strategies to mitigate DOX-related endocrine damage.

## Conclusion

This study provides the first systematic evidence that DOX directly compromises thyroid integrity by inducing oxidative stress, mitochondrial dysfunction, and subsequent impairment of hormone regulation, as demonstrated in both primary thyroid follicular cells and zebrafish models (Figure 10). These findings identify the thyroid as a previously overlooked target of DOX toxicity, thereby extending the recognized spectrum of anthracycline-induced organ damage. Clinically, they underscore the importance of thyroid function monitoring in patients

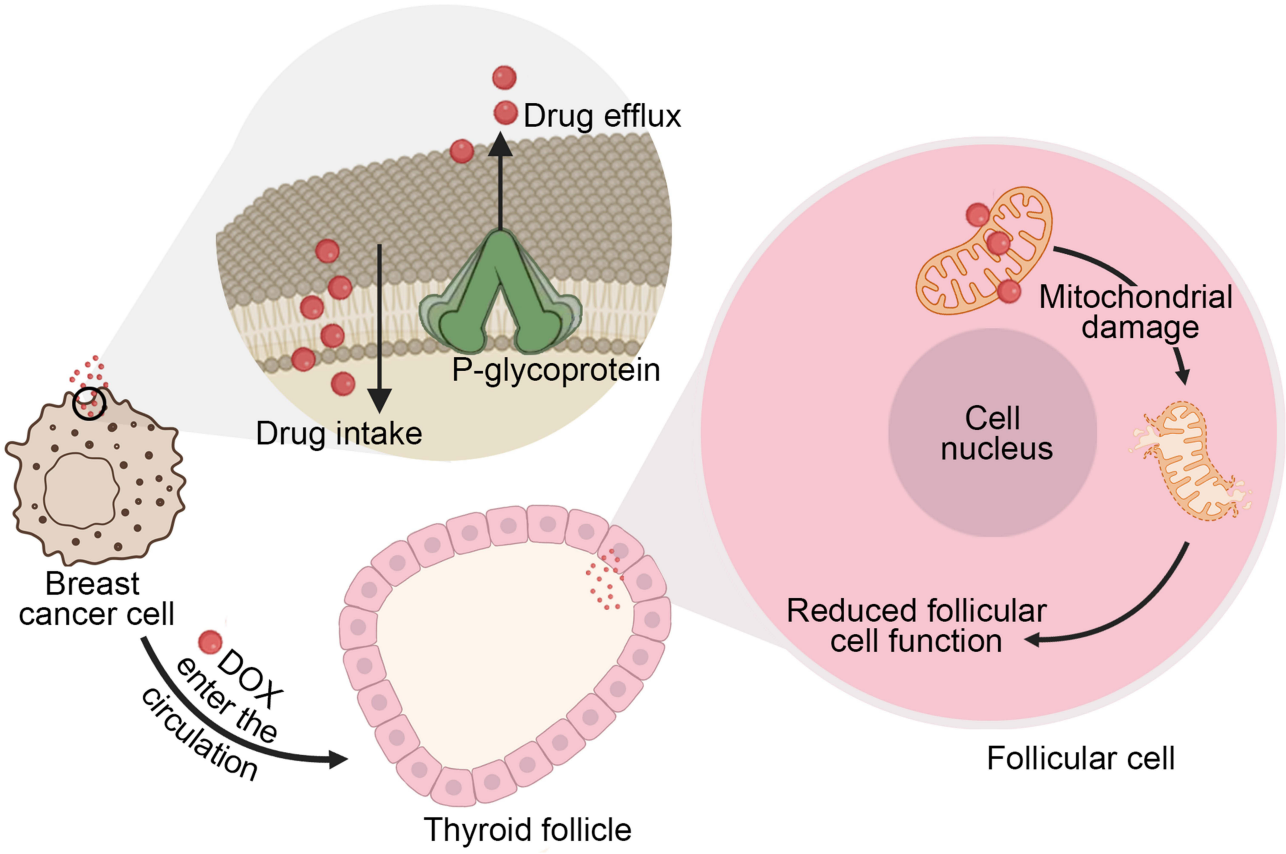


**Figure 10** DOX induces thyroid injury primarily through mitochondrial damage.

receiving DOX-based chemotherapy and point to the need for developing protective strategies to mitigate endocrine side effects. Nevertheless, certain limitations must be acknowledged. Our study primarily relies on in vitro primary thyroid follicular cells and zebrafish models. While these models are effective for dissecting direct DOX-thyroid interactions, they cannot fully recapitulate the complex physiological milieu of human patients. Overall, this work establishes a novel paradigm for understanding DOX-induced endocrine toxicity and advocates for proactive clinical management to safeguard thyroid health in oncology patients.

## Data Sharing Statement

Data will be made available on request.

## Ethics Statement

Animal experiments were approved by the Animal Research Ethical Review Committee of Wenzhou University (Ethics No. WZU-2025-130) and were conducted in full accordance with the National Standard GB/T35892-2018 (Laboratory Animal-Guideline for Ethical Review of Animal Welfare) of the People's Republic of China.

## Author Contributions

All authors made a significant contribution to the work reported, whether that is in the conception, study design, execution, acquisition of data, analysis and interpretation, or in all these areas; took part in drafting, revising or critically reviewing the article; gave final approval of the version to be published; have agreed on the journal to which the article has been submitted; and agree to be accountable for all aspects of the work.


https://doi.org/10.2147/DDDT.S576622

## Funding

This work was supported by the Zhejiang Province Medical and Health Science and Technology Plan Project (2024KY1239), Wenzhou Science and Technology Plan Project (Y2023107), Talent Launch Project of Wenzhou Medical University (KYYW202434), Scientific Research Cultivation Project of the College of Life and Environmental Sciences, Wenzhou University (SHPY2025010).

## Disclosure

The authors declare that they have no known competing financial interests or personal relationships that could have appeared to influence the work reported in this paper.

## References

1. Wu J, Chen J, Feng Y. et al. An immune cocktail therapy to realize multiple boosting of the cancer-immunity cycle by combination of drug/gene delivery nanoparticles. *Sci Adv*. 2020;6(40):7828. doi:10.1126/sciadv.abc7828
2. Lee MJ, Ye AS, Gardino AK, et al. Sequential application of anticancer drugs enhances cell death by rewiring apoptotic signaling networks. *Cell*. 2012;149(4):780–794. doi:10.1016/j.cell.2012.03.031
3. Chiche A, Le Roux I, von Joest M, et al. Injury-Induced Senescence Enables In Vivo Reprogramming in Skeletal Muscle. *Cell Stem Cell*. 2017;20 (3):407–414.e4. doi:10.1016/j.stem.2016.11.020
4. Reynolds JG, Geretti E, Hendriks BS, et al. HER2-targeted liposomal doxorubicin displays enhanced anti-tumorigenic effects without associated cardiotoxicity. *Toxicol Appl Pharmacol*. 2012;262(1):1–10. doi:10.1016/j.taap.2012.04.008
5. Li M, Tang Z, Lv S, et al. Cisplatin crosslinked pH-sensitive nanoparticles for efficient delivery of doxorubicin. *Biomaterials*. 2014;35 (12):3851–3864. doi:10.1016/j.biomaterials.2014.01.018
6. Mehra NK, Verma AK, Mishra PR, Jain NK. The cancer targeting potential of D-α-tocopheryl polyethylene glycol 1000 succinate tethered multi walled carbon nanotubes. *Biomaterials*. 2014;35(15):4573–4588. doi:10.1016/j.biomaterials.2014.02.022
7. Zhu Z, Zhai Y, Hao Y, et al. Specific anti-glioma targeted-delivery strategy of engineered small extracellular vesicles dual-functionalised by Angiopep-2 and TAT peptides. *J Extracell Vesicles*. 2022;11(8):e12255. doi:10.1002/jev2.12255
8. Ma ZG, Kong CY, Wu HM, et al. Toll-like receptor 5 deficiency diminishes doxorubicin-induced acute cardiotoxicity in mice. *Theranostics*. 2020;10(24):11013–11025. doi:10.7150/thno.47516
9. Guo L, Zhang Y, Yang Z, et al. Tunneling Nanotubular Expressways for Ultrafast and Accurate M1 Macrophage Delivery of Anticancer Drugs to Metastatic Ovarian Carcinoma. *ACS Nano*. 2019;13(2):1078–1096. doi:10.1021/acsnano.8b08872
10. Hullin R, Métrich M, Sarre A, et al. Diverging effects of enalapril or eplerenone in primary prevention against doxorubicin-induced cardiotoxicity. *Cardiovasc Res*. 2018;114(2):272–281. doi:10.1093/cvr/cvx162
11. Di Jeso B, Arvan P. Thyroglobulin From Molecular and Cellular Biology to Clinical Endocrinology. *Endocr Rev*. 2016;37(1):2–36. doi:10.1210/er.2015-1090
12. Schinner S, Bornstein SR. Cortical-chromaffin cell interactions in the adrenal gland. *Endocr Pathol*. 2005;16(2):91–98. doi:10.1385/ep:16:2:091
13. Han TS, Williams GR, Vanderpump MPJ. Benzofuran derivatives and the thyroid. *Clin Endocrinol*. 2009;70(1):2–13. doi:10.1111/j.1365-2265.2008.03350.x
14. Koenig KL, Goans RE, Hatchett RJ, et al. Medical treatment of radiological casualties: current concepts. *Ann Emerg Med*. 2005;45(6):643–652. doi:10.1016/j.annemergmed.2005.01.020
15. Lee SY, Rhee CM, Leung AM, Braverman LE, Brent GA, Pearce EN. A review: radiographic iodinated contrast media-induced thyroid dysfunction. *J Clin Endocrinol Metab*. 2015;100(2):376–383. doi:10.1210/jc.2014-3292
16. Li Y, Zang Y, Fan T, et al. Transcriptomic signatures associated with autoimmune thyroiditis in papillary thyroid carcinoma and cancer immunotherapy-induced thyroid dysfunction. *Comput Struct Biotechnol J*. 2022;20:2391–2401. doi:10.1016/j.csbj.2022.05.019
17. Forlenza OV, de Paula VJ, Machado-Vieira R, Diniz BS, Gattaz WF. Does lithium prevent Alzheimer's disease? *Drugs Aging*. 2012;29(5):335–342. doi:10.2165/11599180-000000000-00000
18. Iadarola C, Croce L, Quaquarini E, et al. Nivolumab Induced Thyroid Dysfunction: unusual Clinical Presentation and Challenging Diagnosis. *Front Endocrinol*. 2018;9:813. doi:10.3389/fendo.2018.00813
19. Wouters HJCM, Slagter SN, Muller Kobold AC, van der Klauw MM, Wolffenbuttel BHR. Epidemiology of thyroid disorders in the Lifelines Cohort Study (the Netherlands). *PLoS One*. 2020;15(11):e0242795. doi:10.1371/journal.pone.0242795
20. Dvoretsky AG, Tipisova EV, Alikina VA, Elfimova AE, Dvoretsky VG. Thyroid Hormones in Hemolymph of Red King Crabs from the Barents Sea. *Animals*. 2022;12(3). doi:10.3390/ani12030379
21. Girotra M, Hansen A, Farooki A, et al. The Current Understanding of the Endocrine Effects From Immune Checkpoint Inhibitors and Recommendations for Management. *JNCI Cancer Spectr*. 2018;2(3):pky021. doi:10.1093/jncics/pky021
22. Kapelari K, Kirchlechner C, Högler W, Schweitzer K, Virgolini I, Moncayo R. Pediatric reference intervals for thyroid hormone levels from birth to adulthood: a retrospective study. *BMC Endocr Disord*. 2008;8:15. doi:10.1186/1472-6823-8-15
23. Elkamshoushi AM, Omar SS, El Abd AM, Hassan SZ, Sultan EA, Abd Elkawy E. Subclinical atherosclerosis in psoriatic disease: relation to endocan, TNF-α, age of onset, and body fat. *Int J Dermatol*. 2019;58(4):456–464. doi:10.1111/ijd.14290
24. Garduño-Garcia J, Camarillo Romero E, Loe Ochoa A, et al. Thyroid function is associated with insulin resistance markers in healthy adolescents with risk factors to develop diabetes. *Diabetol Metab Syndr*. 2015;7:16. doi:10.1186/s13098-015-0011-x
25. Wang M, Chai L, Zhao H, Wu M, Wang H. Effects of nitrate on metamorphosis, thyroid and iodothyronine deiodinases expression in Bufo gargarizans larvae. *Chemosphere*. 2015;139:402–409. doi:10.1016/j.chemosphere.2015.07.037
26. Carvalho C, Santos RX, Cardoso S, et al. Doxorubicin: the good, the bad and the ugly effect. *Curr Med Chem*. 2009;16(25):3267–3285. doi:10.2174/092986709788803312

27. Crout TM, Lennep DS, Kishore S, Majithia V. Systemic Vasculitis Associated With Immune Check Point Inhibition: analysis and Review. *Curr Rheumatol Rep*. 2019;21(6):28. doi:10.1007/s11926-019-0828-7
28. Petrioli R, Fiaschi AI, Francini E, Pascucci A, Francini G. The role of doxorubicin and epirubicin in the treatment of patients with metastatic hormone-refractory prostate cancer. *Cancer Treat Rev*. 2008;34(8):710–718. doi:10.1016/j.ctrv.2008.05.004
29. Yang L, Song X, Gong T, et al. Development a hyaluronic acid ion-pairing liposomal nanoparticle for enhancing anti-glioma efficacy by modulating glioma microenvironment. *Drug Deliv*. 2018;25(1):388–397. doi:10.1080/10717544.2018.1431979
30. Kawaguchi T, Takemura G, Kanamori H, et al. Prior starvation mitigates acute doxorubicin cardiotoxicity through restoration of autophagy in affected cardiomyocytes. *Cardiovasc Res*. 2012;96(3):456–465. doi:10.1093/cvr/cvs282
31. Xue X, Huang Y, Bo R, et al. Trojan Horse nanotheranostics with dual transformability and multifunctionality for highly effective cancer treatment. *Nat Commun*. 2018;9(1):3653. doi:10.1038/s41467-018-06093-5
32. Bockstaele L, Kooken H, Libert F, et al. Regulated activating Thr172 phosphorylation of cyclin-dependent kinase 4(CDK4): its relationship with cyclins and CDK "inhibitors". *Mol Cell Biol*. 2006;26(13):5070–5085. doi:10.1128/MCB.02006-05
33. Qu J, Fang Y, Tao R, et al. Advancing thyroid disease research: the role and potential of zebrafish model. *Life Sci*. 2024;357:123099. doi:10.1016/j.lfs.2024.123099
34. Godbole A, Lyga S, Lohse MJ, Calebiro D. Internalized TSH receptors en route to the TGN induce local G(s)-protein signaling and gene transcription. *Nat Commun*. 2017;8(1):443. doi:10.1038/s41467-017-00357-2
35. Zhang M, Yang W, Wang P, et al. CCL7 recruits cDC1 to promote antitumor immunity and facilitate checkpoint immunotherapy to non-small cell lung cancer. *Nat Commun*. 2020;11(1):6119. doi:10.1038/s41467-020-19973-6
36. Lee J, Sul HJ, Choi H, Oh DH, Shong M. Loss of thyroid gland circadian PER2 rhythmicity in aged mice and its potential association with thyroid cancer development. *Cell Death Dis*. 2022;13(10):898. doi:10.1038/s41419-022-05342-2
37. Asnani A, Zheng B, Liu Y, et al. Highly potent visnagin derivatives inhibit Cyp1 and prevent doxorubicin cardiotoxicity. *JCI Insight*. 2018;3(1):96753. doi:10.1172/jci.insight.96753
38. Ai S, Jia T, Ai W, et al. Targeted delivery of doxorubicin through conjugation with EGF receptor-binding peptide overcomes drug resistance in human colon cancer cells. *Br J Pharmacol*. 2013;168(7):1719–1735. doi:10.1111/bph.12055
39. Furukawa T, Komatsu M, Ikeda R, Tsujikawa K, Ichi AS. Copper transport systems are involved in multidrug resistance and drug transport. *Curr Med Chem*. 2008;15(30):3268–3278. doi:10.2174/092986708786848479
40. Han K, Zhu JY, Jia HZ, et al. Mitochondria-Targeted Chimeric Peptide for Trinitarian Overcoming of Drug Resistance. *ACS Appl Mater Interfaces*. 2016;8(38):25060–25068. doi:10.1021/acsami.6b06522
41. Yu H, Li JM, Deng K, et al. Tumor acidity activated triphenylphosphonium-based mitochondrial targeting nanocarriers for overcoming drug resistance of cancer therapy. *Theranostics*. 2019;9(23):7033–7050. doi:10.7150/thno.35748
42. Xiong H, Ni J, Jiang Z, Tian F, Zhou J, Yao J. Intracellular self-disassemble polysaccharide nanoassembly for multi-factors tumor drug resistance modulation of doxorubicin. *Biomater Sci*. 2018;6(9):2527–2540. doi:10.1039/c8bm00570b
43. Václavíková R, Kondrová E, Ehrlichová M, et al. The effect of flavonoid derivatives on doxorubicin transport and metabolism. *Bioorg Med Chem*. 2008;16(4):2034–2042. doi:10.1016/j.bmc.2007.10.093
44. Cottage CT, Neidig L, Sundararaman B, et al. Increased mitotic rate coincident with transient telomere lengthening resulting from pim-1 overexpression in cardiac progenitor cells. *Stem Cells*. 2012;30(11):2512–2522. doi:10.1002/stem.1211
45. Volkova M, Palmeri M, Russell KS, Russell RR. Activation of the aryl hydrocarbon receptor by doxorubicin mediates cytoprotective effects in the heart. *Cardiovasc Res*. 2011;90(2):305–314. doi:10.1093/cvr/cvr007
46. An P, Fan D, Guo Z, et al. Bone morphogenetic protein 10 alleviates doxorubicin-induced cardiac injury via signal transducer and activator of transcription 3 signaling pathway. *Bioengineered*. 2022;13(3):7471–7484. doi:10.1080/21655979.2022.2048994
47. Chakraborty C, Sharma AR, Sharma G, Lee SS. Zebrafish: a complete animal model to enumerate the nanoparticle toxicity. *J Nanobiotechnology*. 2016;14(1):65. doi:10.1186/s12951-016-0217-6
48. Wang X, Geng X, Yang L, et al. Total and Mitochondrial Transcriptomic and Proteomic Insights into Regulation of Bioenergetic Processes for Shoot Fast-Growth Initiation in Moso Bamboo. *Cells*. 2022;11(7). doi:10.3390/cells11071240
49. Wiedemann N, Urzica E, Guiard B, et al. Essential role of Isd11 in mitochondrial iron-sulfur cluster synthesis on Isu scaffold proteins. *EMBO J*. 2006;25(1):184–195. doi:10.1038/sj.emboj.7600906
50. Tank EM, Figueroa-Romero C, Hinder LM, et al. Abnormal RNA stability in amyotrophic lateral sclerosis. *Nat Commun*. 2018;9(1):2845. doi:10.1038/s41467-018-05049-z
51. Yu T, Sheu SS, Robotham JL, Yoon Y. Mitochondrial fission mediates high glucose-induced cell death through elevated production of reactive oxygen species. *Cardiovasc Res*. 2008;79(2):341–351. doi:10.1093/cvr/cvn104
52. Alhowail AH. Pioglitazone ameliorates doxorubicin-induced hypothyroidism and cardiotoxicity in rat models. *Eur Rev Med Pharmacol Sci*. 2023;27(19):9388–9395. doi:10.26355/eurrev_202310_33966
53. Alotayk LI, Aldubayan MA, Alenezi SK, Anwar MJ, Alhowail AH. Comparative evaluation of doxorubicin, cyclophosphamide, 5-fluorouracil, and cisplatin on cognitive dysfunction in rats: delineating the role of inflammation of hippocampal neurons and hypothyroidism. *Biomed Pharmacother*. 2023;165:115245. doi:10.1016/j.biopha.2023.115245
54. Babalola AA, Da-silva OF, Adelowo AR, Adedara IA, Farombi EO. Diphenyl Diselenide Mitigates Renal and Thyroid Dysfunction Associated With Doxorubicin Administration in Wistar Rats. *J Biochem Mol Toxicol*. 2025;39(8):e70431. doi:10.1002/jbt.70431